

# Free-surface flow modeling and simulation of horizontal-axis tidal-stream turbines



J. Yan, X. Deng, A. Korobenko, Y. Bazilevs\*

Department of Structural Engineering, University of California, San Diego, 9500 Gilman Drive, Mail Code 0085, La Jolla, CA 92093, USA

## ARTICLE INFO

### Article history:

Received 20 April 2016

Revised 15 June 2016

Accepted 17 June 2016

Available online 23 June 2016

### Keywords:

Free-surface flow

Tidal energy

ALE-VMS

Horizontal-axis tidal-stream turbines (HATTs)

Level-set redistancing

## ABSTRACT

A computational free-surface flow framework that enables 3D, time-dependent simulation of horizontal-axis tidal-stream turbines (HATTs) is presented and deployed using a complex-geometry HATT. Free-surface flow simulations using the proposed framework, without any empiricism, are able to accurately capture the effect of the free surface on the hydrodynamic performance of the turbine, as demonstrated through excellent agreement with the experimental data. To carry out the free-surface computations, we have developed a novel level-set redistancing procedure compatible with the sliding-interface technique used for handling the rotor-stator interaction in the HATT full-machine simulations. To illustrate the versatility of the proposed approach, additional computations are carried out where the HATT is subjected to wave action.

© 2016 Elsevier Ltd. All rights reserved.

## 1. Introduction

Renewable energy technologies based on wind and solar energy heavily rely on the weather, which, depending on the geographical location, may exhibit high degree of unpredictability or temporal variation. In contrast, tidal currents present a more predictable resource of renewable energy, and, in recent years, a number of technologies have been developed in the academic and commercial sectors that enable conversion of the energy available within tidal currents into electrical power [38,41,49,50,56,63]. Among them, horizontal-axis tidal-stream turbines (HATTs) present the most mature and promising technology. Examples of HATTs include a twin-rotor SeaGen turbine from Marine Current Turbine that is currently undergoing testing near the coast of Northern Ireland [1], and a single-rotor turbine from Verdant Power that has been operating successfully in the East River near New York City [2,36,40,53].

Current research on HATTs is mostly focused on improving their power-generation efficiency. As a result, numerous computational and experimental approaches have been proposed and explored to accurately predict and improve their hydrodynamic performance [9,10,12–14]. Although HATTs make use of the same mechanical principles as the horizontal-axis wind turbines (HAWTs), there are a number of fundamental differences between the two, especially when it comes to modeling and simulation challenges involved. In particular, HATTs are subjected to

hydrodynamic loading (in contrast to HAWTs that are subjected to aerodynamic loading), the effect of free surface becomes important for the cases of shallow-tip immersion, and cavitation may occur for the cases of higher flow and rotor speeds.

Traditionally, reduced-order numerical techniques such as the vortex-element and blade-element-momentum methods have been used to predict the performance of tidal stream turbines [11,54,55,57,58]. Although results from these numerical simulations were occasionally shown to be in good agreement with experimental measurements, the aforementioned methods rely on empirical correlations and may not be suitable for a wide range of operating conditions. Furthermore, due to the computational challenges involved, only a few of the numerical studies considered the free-surface effect, which, as shown in the experimental studies of [7,8], can significantly affect the performance of HATTs. Finally, the analyses presented focused on the rotor only, without taking into account the other turbine components, such as the tower and nacelle.

In this paper, we present our computational free-surface flow framework that enables 3D, time-dependent simulation of HATTs. In addition, we make use of the framework to investigate how the presence of the free surface affects the HATT hydrodynamic performance. The level-set method [3–5,48,60,61] is adopted to track the evolution of the free surface, which is treated as an air-water interface. The aerodynamics and hydrodynamics are governed by the Navier–Stokes equations of incompressible, two-fluid flows, in which the fluid density and viscosity are defined by means of the level-set function. The finite-element-based

\* Corresponding author.

E-mail address: [yuri@ucsd.edu](mailto:yuri@ucsd.edu) (Y. Bazilevs).

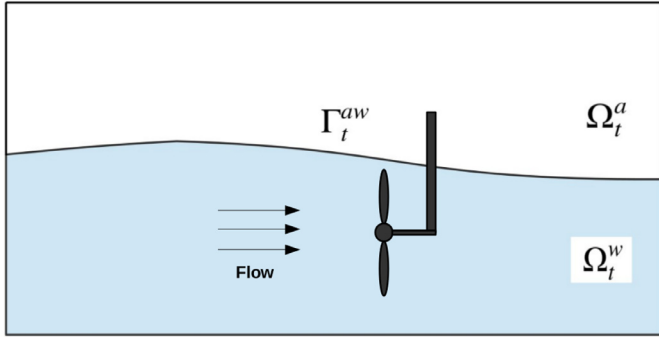


Fig. 1. Illustration of the problem spatial domain separated by the free surface into air and water subdomains.

Arbitrary Lagrangian–Eulerian Variational Multiscale (ALE–VMS) [21,30,31,33,66–68] formulation enhanced with weakly enforced of essential boundary conditions [15,22,28] is employed to discretize the free-surface flow equations. The sliding-interface formulation [23] is employed to account for the presence of tower and nacelle, thus enabling the so-called “full machine” simulation [43]. The sliding-interface formulation is augmented to include level-set re-distancing. This augmentation of the sliding-interface formulation is reported for the first time, and presents a stable and robust technology that allows the air–water interface to cross the sliding interface. The overall method is in the framework of the Mixed Interface-Tracking/Interface-Capturing Technique (MITICT) [86,88], which was primarily introduced for fluid–object interaction with multiple fluids [73,74].

In Section 2 we introduce the governing free-surface-flow equations at the continuous level, summarize the key ingredients of the discrete free-surface-flow formulation, and present the sliding-interface level-set formulation with re-distancing. In Section 3 we describe the HATT design employed in the present work, and present simulation results corresponding to different inflow conditions and tip-immersion depths. In Section 4 we draw conclusions.

## 2. Free-surface flow modeling and simulation

### 2.1. Governing equations of free-surface incompressible flows

We summarize the governing differential equations of free-surface flow posed on a moving domain. Let  $\Omega_t \in \mathbb{R}^d$ ,  $d = 2, 3$  denote the combined air–water domain at time  $t$  and let  $\Gamma_t$  denote its boundary. The domain  $\Omega_t$  is decomposed into the water and air subdomains denoted by  $\Omega_t^w$  and  $\Omega_t^a$ , respectively, while  $\Gamma_t^{aw}$  denotes the interface between them. (See Fig. 1 for an illustration.) We utilize the level-set method for incompressible two-fluid flows [3–5,48,60,61], and introduce a scalar level-set function  $\phi : \Omega_t \rightarrow \mathbb{R}$ , which divides the spatial domain into the air and water subdomains and their interface as follows:

$$\Omega_t^a = \{\mathbf{x} | \phi(\mathbf{x}, t) < 0, \forall \mathbf{x} \in \Omega_t\}, \quad (1)$$

$$\Omega_t^w = \{\mathbf{x} | \phi(\mathbf{x}, t) > 0, \forall \mathbf{x} \in \Omega_t\}, \quad (2)$$

$$\Gamma_t^{aw} = \{\mathbf{x} | \phi(\mathbf{x}, t) = 0, \forall \mathbf{x} \in \Omega_t\}. \quad (3)$$

The Navier–Stokes equations of incompressible two-fluid flows on a moving domain may be stated using the ALE description [46] as

$$\rho \left( \frac{\partial \mathbf{u}}{\partial t} \Big|_{\hat{\mathbf{x}}} + (\mathbf{u} - \hat{\mathbf{u}}) \cdot \nabla \mathbf{u} - \mathbf{f} \right) - \nabla \cdot \boldsymbol{\sigma} = \mathbf{0} \text{ in } \Omega_t, \quad (4)$$

$$\nabla \cdot \mathbf{u} = 0 \text{ in } \Omega_t, \quad (5)$$

where  $\mathbf{f}$  is the body force per unit fluid mass,  $\hat{\mathbf{u}}$  is the velocity of the fluid domain,  $\nabla^s$  is the symmetric gradient operator,  $\boldsymbol{\sigma}$  is the Cauchy stress defined by  $\boldsymbol{\sigma}(\mathbf{u}, p) = -p\mathbf{I} + 2\mu\nabla^s\mathbf{u}$ , and  $\mathbf{u}$  and  $p$  are the fluid velocity and pressure, respectively. The fluid density  $\rho$  and dynamic viscosity  $\mu$  of each spatial point are assigned as follows:

$$\rho = \rho_w H(\phi) + \rho_a (1 - H(\phi)), \quad (6)$$

$$\mu = \mu_w H(\phi) + \mu_a (1 - H(\phi)), \quad (7)$$

where  $H(\phi)$  is the Heaviside function defined by

$$H(\phi) = \begin{cases} 0 & \text{if } \phi < 0, \\ 1/2 & \text{if } \phi = 0, \\ 1 & \text{if } \phi > 0, \end{cases} \quad (8)$$

and where the subscripts  $a$  and  $w$  refer to the quantities defined for the air and water subdomain, respectively.

The air–water interface is assumed to move with the fluid material particles, which is modeled by means of a convection equation for the level-set function  $\phi$ , also posed on a moving domain in the ALE description and written as

$$\frac{\partial \phi}{\partial t} \Big|_{\hat{\mathbf{x}}} + (\mathbf{u} - \hat{\mathbf{u}}) \cdot \nabla \phi = 0 \text{ in } \Omega_t. \quad (9)$$

In the above differential equations, the partial time derivatives are taken holding the referential coordinates  $\hat{\mathbf{x}}$  fixed. The space derivatives are taken holding the current-configuration spatial coordinates  $\mathbf{x}$  fixed. Provided the appropriate initial and boundary conditions are set, and the motion of the fluid mechanics domain is prescribed, the above equations constitute a complete mathematical model of the free-surface flow on a moving domain at the continuous level.

### 2.2. Discretization methods

To discretize the free-surface equations, the ALE–VMS method [21,66] and weak enforcement of essential boundary conditions [19,22,28,29,42], which have been applied to a variety of challenging fluid mechanics and fluid–structure interaction problems in [6,25–27,30,31,33,34,91,92], are employed in the present work.

In order to simulate the full tidal-stream turbine configuration, which includes the spinning rotor and stationary nacelle and tower, the sliding-interface method is employed. The approach utilizes a moving subdomain, which encloses the spinning rotor, and a stationary subdomain, which contains the rest of the tidal turbine (See Fig. 2). The two domains are in relative motion and share a sliding cylindrical interface. Because the meshes on each side of the interface are nonmatching due to relative motion of the subdomains, the kinematic, level-set, and traction compatibility conditions are enforced in the weak sense. The sliding-interface technique was originally developed in [23] in the context of Iso-geometric Analysis (IGA) [39,45], and successfully applied to simulate offshore wind turbines in [24,43,51,52], hydraulic arresting gears in [90], and kayak propulsion in [91]. The sliding-interface formulation was recently extended to the space–time (ST) VMS method [70,72,75–78,80], and the extension is called the “ST Slip Interface (ST-SI)” method [79,82,84,85].

In the present work, the spatial discretization makes use of linear finite elements, and the generalized- $\alpha$  method [16,37,47] is employed to advance the solution in time. A two-stage predictor–multicorrector algorithm based on Newton’s method is used to solve the nonlinear equations arising in the level-set formulation. At each Newton iteration a flexible GMRES algorithm [64,65] is employed to solve the coupled linear-equation systems. GMRES

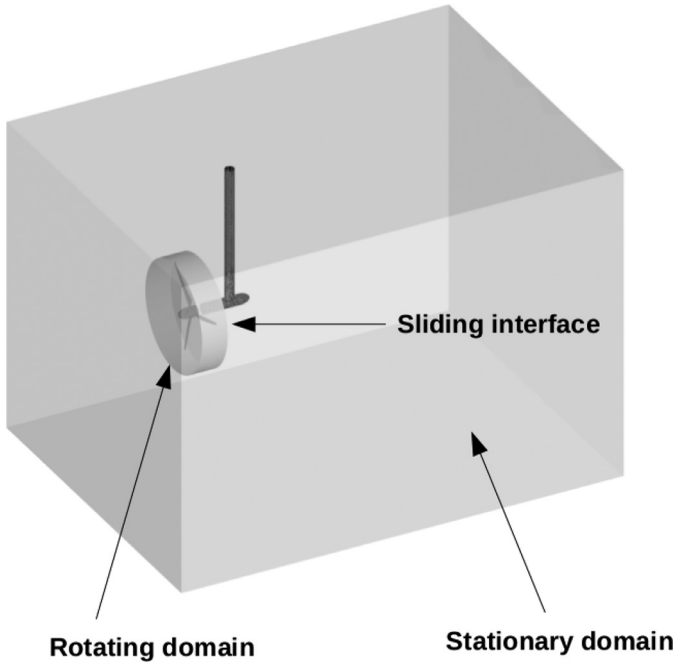


Fig. 2. Illustration of the problem spatial domain and sliding interface.

is preconditioned using iterative solution of individual, linearized fluid-mechanics and level-set problems, as proposed in [92].

### 2.3. Level-set redistancing in the presence of sliding interfaces

In discrete setting, instead of using Eq. (8) to distribute the density and viscosity properties to the two-fluid medium, we employ the following *regularized* version of the Heaviside function:

$$H_\epsilon(\phi) = \begin{cases} 0 & \text{if } \phi < -\epsilon, \\ \frac{1}{2} \left( 1 + \frac{\phi}{\epsilon} + \frac{1}{\pi} \sin\left(\frac{\phi\pi}{\epsilon}\right) \right) & \text{if } |\phi| \leq \epsilon, \\ 1 & \text{if } \phi > \epsilon. \end{cases} \quad (10)$$

Here  $\epsilon$  is assumed to scale with the local mesh size, and defines the interface width between the air and water subdomains. As the mesh is refined,  $\epsilon \rightarrow 0$ , and  $H_\epsilon$  approaches its “sharp” counterpart given by Eq. (8).

Regularizing the Heaviside function leads to a smooth transition of the material properties between the air and water subdomain, which is numerically more advantageous than a sharp discontinuity in the material parameters. However, this regularization requires that the level-set function  $\phi$  satisfies the signed-distance property, at least in the interface layer between the two fluids. To enforce the signed-distance property, we define an additional level-set field  $\phi_d$  that satisfies the Eikonal partial differential equation,

$$||\nabla\phi_d|| = 1 \text{ in } \Omega_t, \quad (11)$$

together with the interior constraint,

$$\phi_d = \phi = 0 \text{ on } \Gamma_t^{aw}. \quad (12)$$

In order to satisfy Eqs. (11) and (12), we introduce a pseudo-time

variable  $\tilde{t}$ , and make use of the following semi-discrete form of the Eikonal equation: Given  $\phi^h$ , find  $\phi_d^h$ , such that  $\forall \eta^h$ ,

$$\begin{aligned} & \int_{\Omega_t} \eta^h \left( \frac{\partial \phi_d^h}{\partial \tilde{t}} + \mathbf{a}^h \cdot \nabla \phi_d^h - S_\epsilon(\phi_d^h) \right) d\Omega \\ & + \int_{\Omega_t} \tau \mathbf{a}^h \cdot \nabla \eta^h \left( \frac{\partial \phi_d^h}{\partial \tilde{t}} + \mathbf{a}^h \cdot \nabla \phi_d^h - S_\epsilon(\phi_d^h) \right) d\Omega \\ & + \int_{\Omega_t} \eta^h \lambda_{pen} \frac{dH_\epsilon}{d\phi} (\phi_d^h - \phi^h) d\Omega \\ & - \int_{(\Gamma_t)_{SI}} \eta_s^h [\mathbf{a}_s^h \cdot \mathbf{n}_s]_- (\phi_{d,s}^h - \phi_{d,m}^h) d\Gamma \\ & - \int_{(\Gamma_t)_{SI}} \eta_m^h [\mathbf{a}_m^h \cdot \mathbf{n}_m]_- (\phi_{d,m}^h - \phi_{d,s}^h) d\Gamma = 0, \end{aligned} \quad (13)$$

where  $\mathbf{a}^h = S_\epsilon(\phi_d^h) \nabla \phi_d^h / ||\nabla \phi_d^h||$  is the effective “convective” velocity and  $S_\epsilon(\phi_d^h) = 2H_\epsilon(\phi_d^h) - 1$  is the regularized sign function. The first three terms on the left hand side of the above semi-discrete formulation correspond to the SUPG formulation [35] of the pseudo-time-dependent Eikonal equation with the interior constraint handled through a penalty technique, as proposed in earlier references [3–5]. In these terms,  $\tau$  is the usual stabilization parameter [44,62,81,83,87,89] and  $\lambda_{pen}$  is the mesh-size-independent penalty constant. The last two terms on the left hand side of Eq. (13) weakly enforce the continuity of  $\phi_d^h$  across the sliding interface denoted by  $(\Gamma_t)_{SI}$ . In these terms subscripts *s* and *m* denote stationary and moving parts of the sliding interface, respectively,  $[\cdot]_-$  gives the negative part of the bracketed quantity, and  $\mathbf{n}$  is the unit outward normal vector.

At the end of each physical time step, the level-set field is redistanced, that is, Eq. (13) is integrated in pseudo-time using the Backward Euler method, which gives a new level set field  $\phi_d^h$  with the signed-distance property and zero level set coincident with that of  $\phi^h$ .

## 3. Numerical results

We first describe the HATT geometry employed in this work. We then present uniform-inflow simulations to assess the accuracy performance of the proposed free-surface flow framework through experimental validation. Finally, we report additional simulations to show how the HATT responds to wave action.

### 3.1. HATT geometry

The tidal turbine rotor used in the present simulations is taken from [8], which is a three-blade design with a 20° hub-pitch angle. This rotor is widely used for validation of numerical methods for tidal energy, largely because of the availability of experimental data characterizing its hydrodynamic performance in the presence of the free surface [7,8]. The rotor diameter  $D = 0.8$  m, and the blade geometry is comprised of NACA 63-812, NACA 63-815, NACA 63-818, NACA 63-821 and NACA 63-824 airfoil cross-section shapes. The 3D rotor blades are constructed by stacking the appropriately scaled, offset, and twisted 2D cross-sections, much like is done in the case of wind-turbine blades [18,20,69,71,83]. The resulting rotor surface model is shown in Fig. 3.

### 3.2. Uniform-inflow simulations

For uniform inflow conditions, we perform both pure hydrodynamics and free-surface simulations. In the case of pure hydrodynamics simulation the tidal turbine is fully immersed in the water domain, and the free-surface effect is neglected. The computational

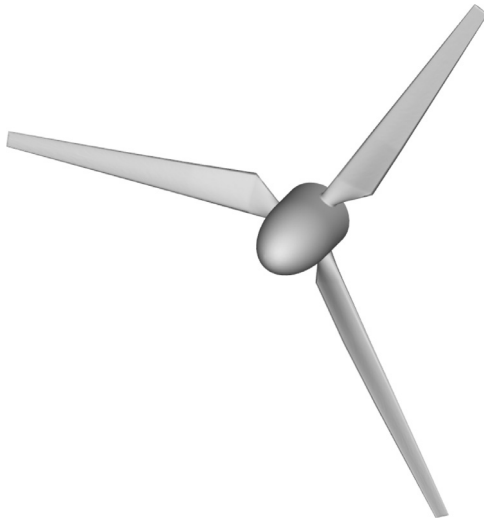


Fig. 3. HATT surface model employed in the present work.

domain for the pure hydrodynamics simulation is a box with dimensions  $4.35 \text{ m} \times 2.8 \text{ m} \times 2.64 \text{ m}$ . A refined cylinder with length of 2 m and radius of 0.5 m is added to capture the turbulent wake generated by the turbine. As shown in Fig. 4, the domain is divided into two subdomains separated by a cylindrical sliding interface. The volume mesh makes use of the triangular prisms in the rotor boundary layers and tetrahedra elsewhere. The planar cut of the 3D mesh is shown in Fig. 4. The mesh statistics and element lengths employed in the pure hydrodynamics simulation case are summarized in Tables 1 and 2.

The computational domain of the free-surface simulations is a box with dimensions  $6.6 \text{ m} \times 2.8 \text{ m} \times 4.14 \text{ m}$ . The sliding interface and refined cylinder for capturing the wake are the same as in the pure hydrodynamics simulation. In addition, as shown in Fig. 5, another refined box is built around the still water level to

**Table 1**  
Mesh statistics for the pure hydrodynamics simulation.

Number of nodes	Number of elements
709,143	3,660,467

**Table 2**  
Element sizes employed for the pure hydrodynamics simulation (in m).

Outer boundary	Wake refinement box	Rotor boundary layer
0.5	0.02	0.0005

**Table 3**  
Mesh statistics for free-surface simulations.

Number of nodes	Number of elements
1,339,891	7,389,215

better capture the free-surface evolution. The mesh statistics and element lengths employed in free-surface simulations are summarized in Tables 3 and 4.

Boundary conditions in the computations are specified as follows. For the pure hydrodynamics simulation, uniform inflow velocity is imposed strongly at the inlet; The outlet is open to the hydrostatic-pressure boundary conditions; No-penetration boundary condition is applied on the remaining outer surfaces of the computational domain. For the free-surface simulations, zero wind velocity is applied strongly on the air portion of the inlet, while the desired uniform flow velocity is applied strongly on the water portion of the inlet; the level-set field is also prescribed strongly on the inlet boundary as a linear function of the vertical coordinate. The zero of this function defines the location of the air-water interface; The top and outlet surfaces are open to the hydrostatic-pressure boundary conditions; No-penetration boundary condition is applied on the lateral and bottom outer surfaces

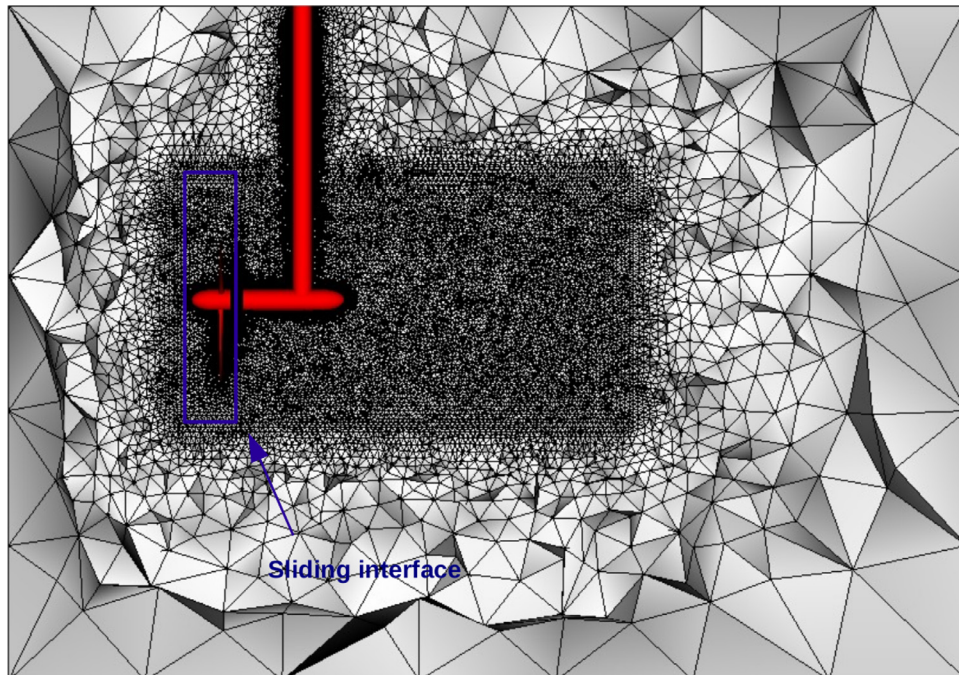
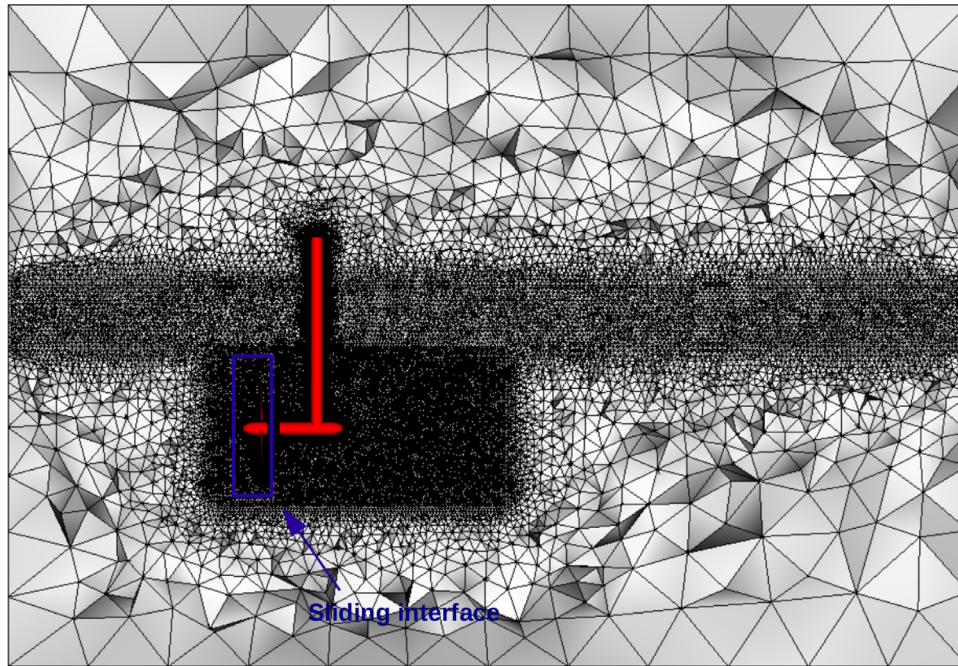
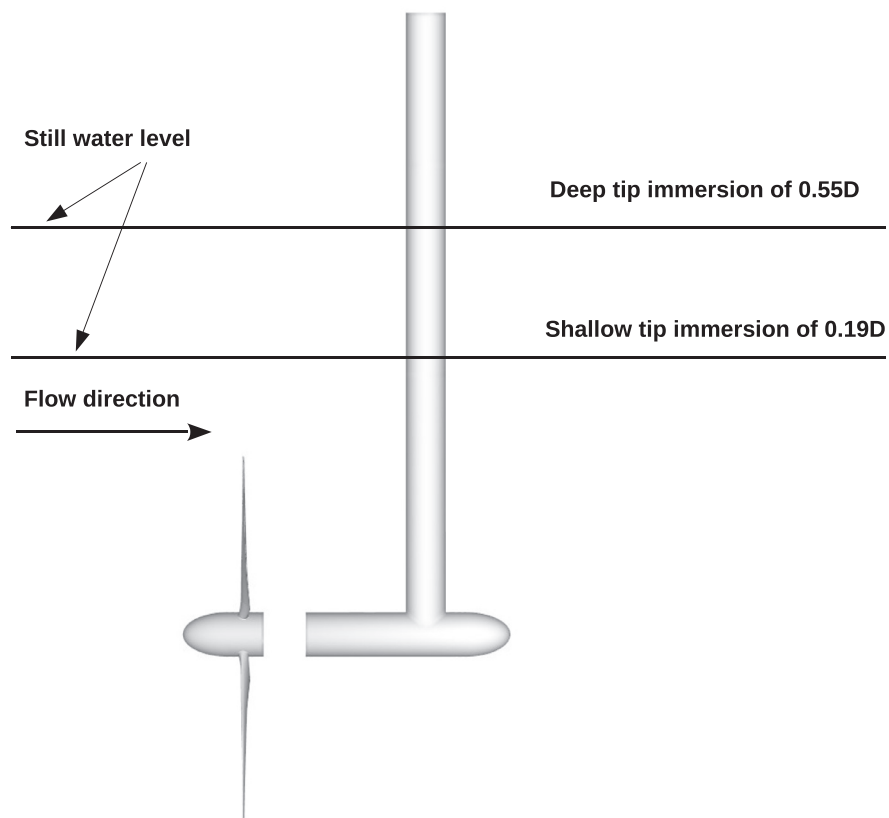


Fig. 4. 2D cut of the computational domain and mesh used in the pure hydrodynamics simulation. The mesh is refined in the inner region for better flow resolution near the tidal stream turbine and its wake.



**Fig. 5.** 2D cut of the computational domain and mesh used in free-surface simulations. Compared to the pure hydrodynamics case, the mesh is also refined to better capture the free surface behavior.



**Fig. 6.** Problem setup.

**Table 4**  
Element sizes employed for free-surface simulations (in m).

Outer boundary	Wake refinement box	Free-surface refinement box	Rotor boundary layer
0.5	0.02	0.03	0.0005

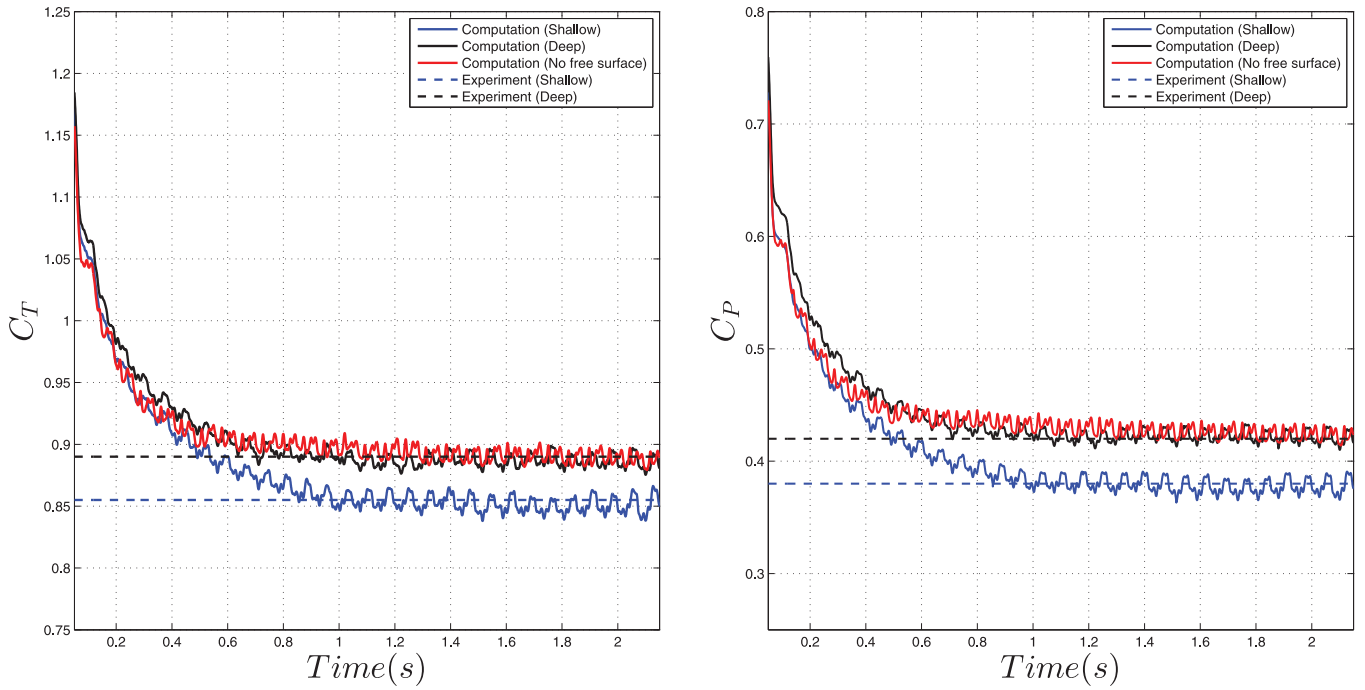


Fig. 7. Time history of the thrust and power coefficients for uniform inflow conditions. Experimental data from [8] is plotted for comparison.

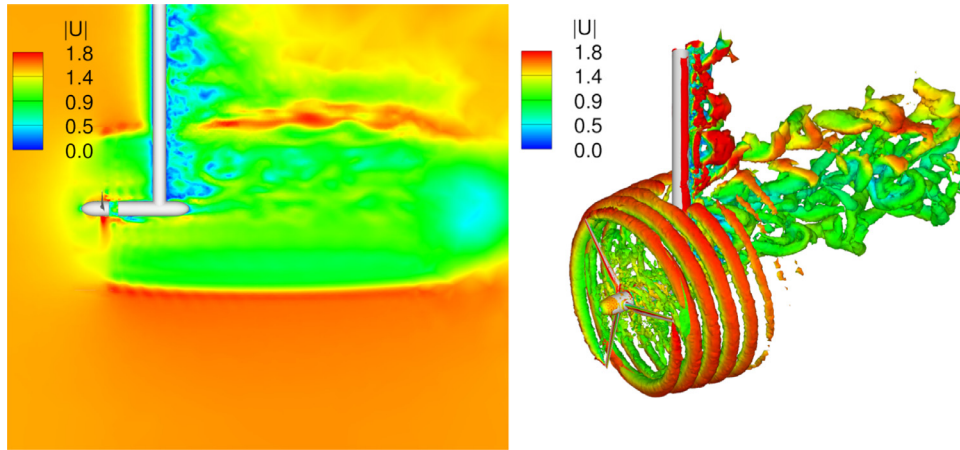


Fig. 8. Pure hydrodynamics simulation. Left: Velocity (in m/s) on a planar cut. Right: Vorticity isosurfaces colored by velocity magnitude (in m/s).

of the computational domain. Backflow stabilization [17,59] is employed on all surfaces where normal velocity is left unspecified.

The rotor speed is set to  $\Omega = 28.1250$  rad/s, and water speed is set to  $U_0 = 1.5$  m/s. We perform one pure hydrodynamics simulation, and two free-surface simulations with deep-tip immersion of  $0.55D$  and shallow-tip immersion of  $0.19D$ . All the simulations are carried out using the time step of  $1 \times 10^{-4}$  s. The problem setup illustrated in Fig. 6.

We report the computed thrust coefficient  $C_T$  and power coefficient  $C_P$ , which are defined as

$$C_T = \frac{4F}{0.5\rho_w\pi D^2U_0^2}, \quad (14)$$

and

$$C_P = \frac{4T\Omega}{0.5\rho_w\pi D^2U_0^3}, \quad (15)$$

where  $F$  and  $T$  are the hydrodynamic thrust force and torque, respectively. The time histories of  $C_T$  and  $C_P$  are compared with experimental data from [8] and shown in Fig. 7. The predicted  $C_T$

and  $C_P$  from the free-surface simulations are in excellent agreement with the experimental data both for shallow- and deep-tip immersion cases. One important trend observed in the experiments [8] and reproduced in the computations is that both coefficients are higher in the deep-tip immersion case. We can also see the  $C_T$  and  $C_P$  values produced by the pure hydrodynamics simulation are very similar to the deep-tip immersion case, suggesting that at that level of immersion the free surface effect is not as important. The results also indicate that the free-surface effect is non-negligible for the shallow-tip immersion case.

Fig. 8 (left) shows velocity magnitude on a planar cut for the pure hydrodynamics simulation, while Fig. 8 (right) shows vorticity isosurfaces colored by velocity magnitude for the same simulation. The solution fields appear to be continuous across the sliding interface, which indicates that the sliding-interface technique is successful for the present application.

Fig. 9 shows the vorticity isosurfaces and free surface colored by the velocity magnitude for both deep- and shallow-tip immersion simulations. In both cases, the air-water interface experiences

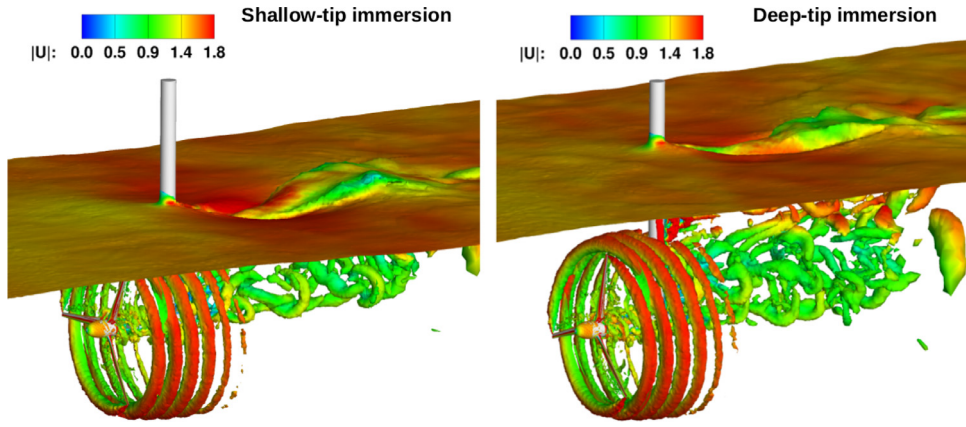


Fig. 9. Snapshots of air-water interface and underwater vorticity colored by velocity magnitude (in m/s) for the free-surface simulation. (For interpretation of the references to color in this figure legend, the reader is referred to the web version of this article.)

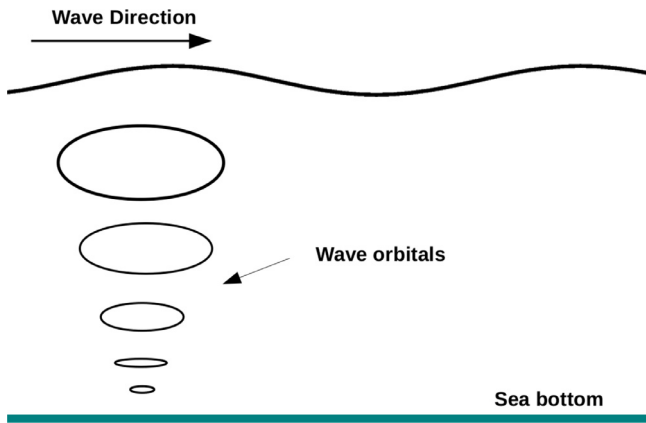


Fig. 10. Structure of the Airy waves where the velocity orbitals, which may be thought of as fluctuations around a uniform profile, have higher amplitude closer to the free surface and gradually decay with depth.

strong topological changes after the flow impacts the tower. The shallow-tip immersion results in larger overall deformation of the

air-water interface, which explains the more pronounced free-surface effect on the thrust and power coefficients in that case.

### 3.3. Airy-wave inflow conditions

We investigate the performance of the same HATT, but in Airy-wave conditions. The simulations presented in this section are outside of the range of experimental data for the tidal turbine considered, and show the versatility of the free-surface flow framework employed. The Airy waves, which may be derived using potential-flow theory, are specified as follows: Given the wave amplitude  $A$ , wave length  $L$ , mean flow speed  $U_0$ , and water depth  $h$ , we define the wavenumber  $k = \frac{2\pi}{L}$  and phase speed  $\omega = \sqrt{gk \tanh(kh)} + kU_0$ . With these definitions, the Airy-wave profile is given by:

$$\phi = A \cos(kx - \omega t) + h - z, \tag{16}$$

$$u = \frac{wA}{\sinh(kh)} \cosh(kz) \cos(kx - \omega t) + U_0, \tag{17}$$

$$v = 0, \tag{18}$$

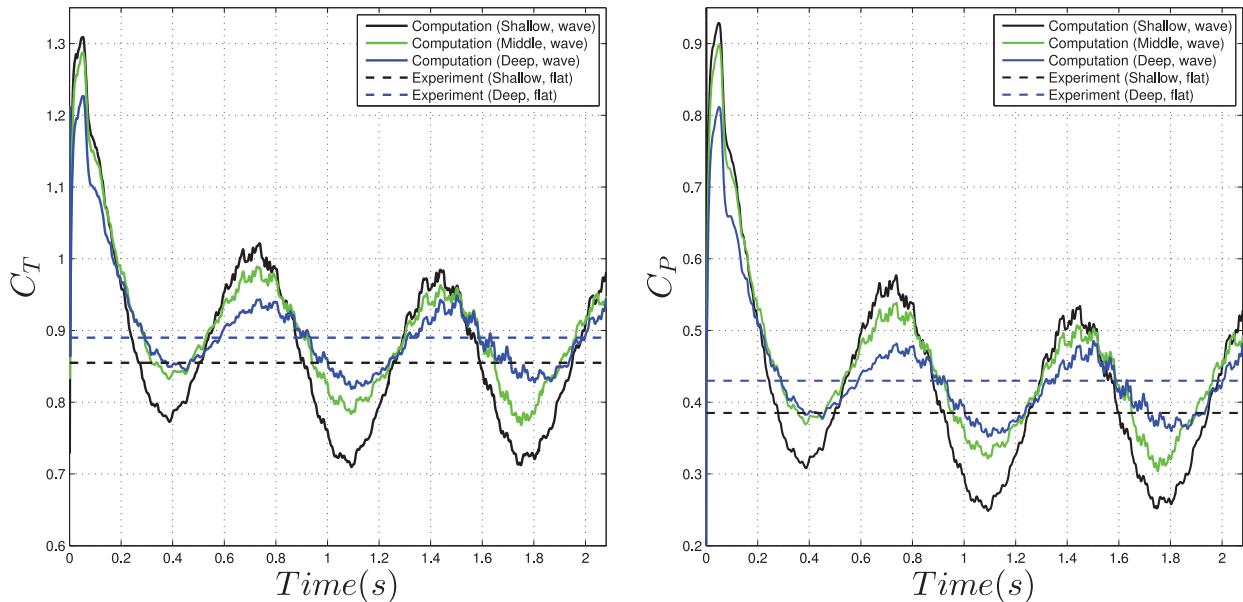
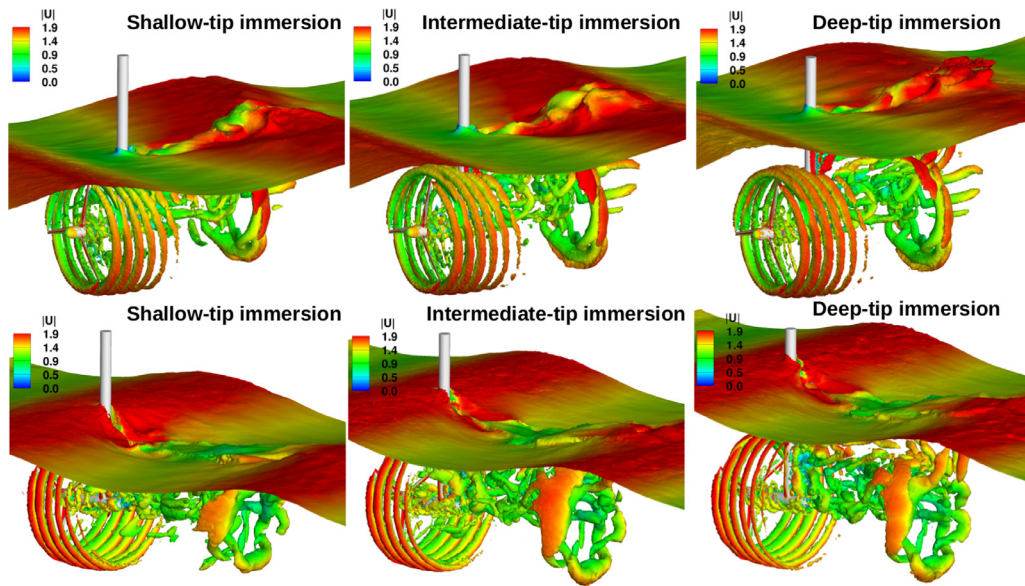


Fig. 11. Time history of the thrust and power coefficients for Airy-wave inflow conditions.



**Fig. 12.** Snapshots of the free surface and underwater vorticity colored by the velocity magnitude (in m/s) for Airy-wave inflow conditions. (For interpretation of the references to color in this figure legend, the reader is referred to the web version of this article.)

**Table 5**

Predicted average values of the thrust and power coefficients, denoted by  $\bar{C}_T$  and  $\bar{C}_p$ , respectively, from the HATT free-surface simulations in Airy-wave conditions.

Cases	$\bar{C}_T$	$\bar{C}_p$
Shallow-tip immersion	0.8513	0.3919
Intermediate-tip immersion	0.8741	0.4141
Deep-tip immersion	0.8794	0.4144

$$w = \frac{wA}{\sinh(kh)} \sinh(kz) \sin(kx - \omega t), \quad (19)$$

where  $(u, v, w)$  are the velocity components. The structure of Airy waves is illustrated in Fig. 10. In the present simulations, we set  $U_0 = 1.5$  m/s,  $H = 0.085$  m, and  $L = 2.4$  m. The rotor speed is the same as in the uniform-flow simulations. The wave profile with the above parameters is strongly imposed at the inlet. The problem domain, mesh, time-step size, and remaining boundary conditions are the same as in the previous section.

Three free-surface simulations with the deep-tip immersion of 0.55 D, shallow-tip immersion of 0.19 D, and intermediate-tip immersion of 0.37 D are performed. The time histories of the thrust and power coefficients are plotted in Fig. 11. The experimental results for the uniform-inflow condition are also plotted for comparison. Because the turbine is now subjected to wave action, the thrust and power coefficients exhibit time-periodic behavior that is consistent with the wave frequency. Due to the structure of Airy waves, we observe higher-amplitude fluctuation of  $C_T$  and  $C_p$  as the turbine is placed closer to the water surface. However, the average values of  $C_T$  and  $C_p$ , listed in Table 5, decrease as the turbine is placed closer to the free surface, which is consistent with the uniform-inflow cases considered in the previous section. We also note that the average values of  $C_T$  and  $C_p$  for intermediate-tip and deep tip immersion cases are very close, which suggests the existence of a minimum immersion depth at which HATTs will operate to their full potential. Fig. 12 shows the flow field with vorticity isosurfaces and the air-water interface colored by velocity magnitude for the three immersion cases, illustrating the complexity of

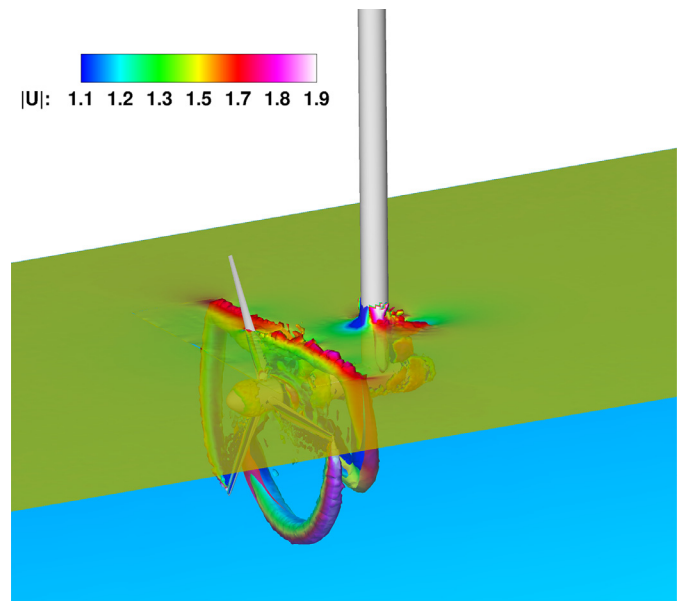


**Fig. 13.** Illustration of a scenario in which the free surface crosses the sliding interface. HATT simulation is carried out wherein rotor blades pierce the water surface. Free surface and vorticity isosurfaces (restricted to the water domain) colored by the flow speed are shown. Free surface exhibits a relatively smooth transition across the sliding interface. (For interpretation of the references to color in this figure legend, the reader is referred to the web version of this article.)

the underlying hydrodynamics and motivating the use of advanced free-surface modeling for the present application.

#### 4. Conclusions

The computational free-surface flow framework that enables 3D, time-dependent simulation of HATTs is presented. The rotor-tower interaction is handled by means of the sliding-interface formulation, while the free-surface modeling makes use of the level-set technique, which includes a so-called redistancing step. In the present work we extend the sliding-interface methodology to

include redistancing, which enables the computation of cases where free surface crosses the sliding interface, as shown in Fig. 13.

The presented computational free-surface flow framework was deployed on a complex-geometry HATT with rotor diameter of 0.8 m. The framework was validated for the cases of uniform flow. In particular, the simulations, without any empiricism, were able to accurately capture the effect of the free surface on the rotor hydrodynamic loading. To illustrate the versatility of the approach, additional computations were carried out where the HATT was subjected to more realistic Airy wave action. These computations revealed the presence of a minimum immersion depth for optimal operation.

fluid-structure interaction (FSI) [32] effects and possible occurrence of cavitation were not considered in the present framework, and are left for future work.

## Acknowledgments

This work was supported by the NSF CAREER No.1055091 and ARO W911NF-14-1-0296 awards. This support is gratefully acknowledged.

## References

- [1] Sea generation, Ltd. <http://www.seageneration.co.uk/>.
- [2] Verdant power, Inc. <http://www.verdantpower.com/>.
- [3] Akkerman I, Bazilevs Y, Benson DJ, Farthing MW, Kees CE. Free-surface flow and fluid-object interaction modeling with emphasis on ship hydrodynamics. *J Appl Mech* 2012;79:010905.
- [4] Akkerman I, Bazilevs Y, Kees CE, Farthing MW. Isogeometric analysis of free-surface flow. *J Comput Phys* 2011;230:4137–52.
- [5] Akkerman I, Dunaway J, Kvandal J, Spinks J, Bazilevs Y. Toward free-surface modeling of planing vessels: simulation of the Fridsma hull using ALE-VMS. *Comput Mech* 2012;50:719–27.
- [6] Augier B, Yan J, Korobenko A, Czarnowski J, Ketterman G, Bazilevs Y. Experimental and numerical FSI study of compliant hydrofoils. *Comput Mech* 2015;55:1079–90. doi:10.1007/s00466-014-1090-5.
- [7] Bahaj A, Batten W, McCann G. Experimental verifications of numerical predictions for the hydrodynamic performance of horizontal axis marine current turbines. *Renew Energ* 2007;32(15):2479–90.
- [8] Bahaj A, Molland A, Chaplin J, Batten W. Power and thrust measurements of marine current turbines under various hydrodynamic flow conditions in a cavitation tunnel and a towing tank. *Renew Energ* 2007;32(3):407–26.
- [9] Bahaj A, Myers L. Fundamentals applicable to the utilisation of marine current turbines for energy production. *Renew Energ* 2003;28(14):2205–11.
- [10] Bai X, Avital E, Munjiza A, Williams J. Numerical simulation of a marine current turbine in free surface flow. *Renew Energ* 2014;63:715–23.
- [11] Baltazar J, De Campos JF. Hydrodynamic analysis of a horizontal axis marine current turbine with a boundary element method. *J Offshore Mech Arct Eng* 2011;133(4):041304.
- [12] Batten W, Bahaj A, Molland A, Chaplin J. Hydrodynamics of marine current turbines. *Renew Energ* 2006;31(2):249–56.
- [13] Batten W, Bahaj A, Molland A, Chaplin J. Experimentally validated numerical method for the hydrodynamic design of horizontal axis tidal turbines. *Ocean Eng* 2007;34(7):1013–20.
- [14] Batten W, Bahaj A, Molland A, Chaplin J. The prediction of the hydrodynamic performance of marine current turbines. *Renew Energ* 2008;33(5):1085–96.
- [15] Bazilevs Y, Calo VM, Cottrell JA, Hughes TJR, Reali A, Scovazzi G. Variational multiscale residual-based turbulence modeling for large eddy simulation of incompressible flows. *Comput Method Appl M* 2007;197:173–201.
- [16] Bazilevs Y, Calo VM, Hughes TJR, Zhang Y. Isogeometric fluid-structure interaction: theory, algorithms, and computations. *Comput Mech* 2008;43:3–37.
- [17] Bazilevs Y, Gohean JR, Hughes TJR, Moser RD, Zhang Y. Patient-specific isogeometric fluid-structure interaction analysis of thoracic aortic blood flow due to implantation of the Jarvik 2000 left ventricular assist device. *Comput Method Appl M* 2009;198:3534–50.
- [18] Bazilevs Y, Hsu M-C, Akkerman I, Wright S, Takizawa K, Henicke B, et al. 3D simulation of wind turbine rotors at full scale. Part I: geometry modeling and aerodynamics. *Int J Numer Meth Fl* 2011;65:207–35. doi:10.1002/ffd.2400.
- [19] Bazilevs Y, Hsu M-C, Benson D, Sankaran S, Marsden A. Computational fluid-structure interaction: methods and application to a total cavopulmonary connection. *Comput Mech* 2009;45:77–89.
- [20] Bazilevs Y, Hsu M-C, Kiendl J, Wüchner R, Bletzinger K-U. 3D simulation of wind turbine rotors at full scale. Part II: Fluid-structure interaction modeling with composite blades. *Int J Numer Meth Fl* 2011;65:236–53.
- [21] Bazilevs Y, Hsu M-C, Takizawa K, Tezduyar TE. ALE-VMS and ST-VMS methods for computer modeling of wind-turbine rotor aerodynamics and fluid-structure interaction. *Math Model Meth Appl Sci* 2012;22(supp02):1230002. doi:10.1142/S0218202512300025.
- [22] Bazilevs Y, Hughes TJR. Weak imposition of Dirichlet boundary conditions in fluid mechanics. *Comput Fluid* 2007;36:12–26.
- [23] Bazilevs Y, Hughes TJR. NURBS-based isogeometric analysis for the computation of flows about rotating components. *Comput Mech* 2008;43:143–150.
- [24] Bazilevs Y, Korobenko A, Deng X, Yan J. Novel structural modeling and mesh moving techniques for advanced FSI simulation of wind turbines. *Int J Numer Meth Eng* 2015;102:766–83. doi:10.1002/nme.4738.
- [25] Bazilevs Y, Korobenko A, Deng X, Yan J. FSI modeling for fatigue-damage prediction in full-scale wind-turbine blades. *J Appl Mech* 2016;83(6):061010.
- [26] Bazilevs Y, Korobenko A, Deng X, Yan J, Kinzel M, Dabiri JO. FSI modeling of vertical-axis wind turbines. *J Appl Mech* 2014;81:081006. doi:10.1115/1.4027466.
- [27] Bazilevs Y, Korobenko A, Yan J, Pal A, Gohari SMI, Sarkar S. ALE-VMS formulation for stratified turbulent incompressible flows with applications. *Math Model Method Appl Sci* 2015;25:1540011.
- [28] Bazilevs Y, Michler C, Calo VM, Hughes TJR. Isogeometric variational multiscale modeling of wall-bounded turbulent flows with weakly enforced boundary conditions on unstretched meshes. *Comput Method Appl M* 2010;199:780–90.
- [29] Bazilevs Y, Michler C, Calo V, Hughes T. Weak dirichlet boundary conditions for wall-bounded turbulent flows. *Comput Method Appl M* 2007;196(49):4853–62.
- [30] Bazilevs Y, Takizawa K, Tezduyar TE. Challenges and directions in computational fluid-structure interaction. *Math Model Method Appl Sci* 2013;23:215–21. doi:10.1142/S0218202513400010.
- [31] Bazilevs Y, Takizawa K, Tezduyar TE. New directions and challenging computations in fluid dynamics modeling with stabilized and multiscale methods. *Math Model Method Appl Sci* 2015;25:2217–26. doi:10.1142/S0218202515020029.
- [32] Bazilevs Y, Takizawa K, Tezduyar TE. Computational fluid-structure interaction: methods and applications. Wiley; February 2013. ISBN 978-0470978771. doi:10.1002/9781118483565.
- [33] Bazilevs Y, Takizawa K, Tezduyar TE, Hsu M-C, Kostov N, McIntyre S. Aerodynamic and FSI analysis of wind turbines with the ALE-VMS and ST-VMS methods. *Arch Comput Method Eng* 2014;21:359–98. doi:10.1007/s11831-014-9119-7.
- [34] Bazilevs Y, Yan J, de Stadler M, Sarkar S. Computation of the flow over a sphere at  $Re = 3700$ : a comparison of uniform and turbulent inflow conditions. *J Appl Mech* 2014;81(12):121003.
- [35] Brooks AN, Hughes TJR. Streamline upwind/Petrov-Galerkin formulations for convection dominated flows with particular emphasis on the incompressible Navier-Stokes equations. *Comput Method Appl M* 1982;32:199–259.
- [36] Charlier R. A “sleeper” awakes: tidal current power. *Renew Sustain Energ Rev* 2003;7(6):515–29.
- [37] Chung J, Hulbert GM. A time integration algorithm for structural dynamics with improved numerical dissipation: the generalized- $\alpha$  method. *J Appl Mech* 1993;60: 371–75.
- [38] Corsini A, Rispoli F, Tezduyar TE. Computer modeling of wave-energy air turbines with the SUPG/PSPG formulation and discontinuity-capturing technique. *J Appl Mech* 2012;79:010910. doi:10.1115/1.4005060.
- [39] Cottrell JA, Hughes TJR, Bazilevs Y. Isogeometric analysis. toward integration of CAD and FEA. Wiley; 2009.
- [40] Fraenkel P. Marine current turbines: pioneering the development of marine kinetic energy converters. *Proc Inst Mech Eng, Part A: J Pow Energ* 2007;221(2):159–69.
- [41] Goundar J, Ahmed M. Design of a horizontal axis tidal current turbine. *Appl Energ* 2013;111:161–74.
- [42] Hsu M-C, Akkerman I, Bazilevs Y. Wind turbine aerodynamics using ALE-VMS: validation and role of weakly enforced boundary conditions. *Comput Mech* 2012;50:499–511.
- [43] Hsu M-C, Bazilevs Y. Fluid-structure interaction modeling of wind turbines: simulating the full machine. *Comput Mech* 2012;50:821–33.
- [44] Hsu M-C, Bazilevs Y, Calo VM, Tezduyar TE, Hughes TJR. Improving stability of stabilized and multiscale formulations in flow simulations at small time steps. *Comput Method Appl Mech Eng* 2010;199:828–40. doi:10.1016/j.cma.2009.06.019.
- [45] Hughes TJR, Cottrell JA, Bazilevs Y. Isogeometric analysis: CAD, finite elements, NURBS, exact geometry, and mesh refinement. *Comput Method Appl Me* 2005;194:4135–95.
- [46] Hughes TJR, Liu WK, Zimmermann TK. Lagrangian-Eulerian finite element formulation for incompressible viscous flows. *Comput Method Appl M* 1981;29:329–49.
- [47] Jansen KE, Whiting CH, Hulbert GM. A generalized- $\alpha$  method for integrating the filtered Navier-Stokes equations with a stabilized finite element method. *Comput Method Appl M* 2000;190(3):305–19.
- [48] Kees CE, Akkerman I, Farthing MW, Bazilevs Y. A conservative level set method suitable for variable-order approximations and unstructured meshes. *J Comput Phys* 2011;230:4536–58.
- [49] Khan M, Bhuyan G, Iqbal M, Quaicoe J. Hydrokinetic energy conversion systems and assessment of horizontal and vertical axis turbines for river and tidal applications: A technology status review. *Appl Energ* 2009;86(10):1823–1835.
- [50] Kolekar N, Banerjee A. Performance characterization and placement of a marine hydrokinetic turbine in a tidal channel under boundary proximity and blockage effects. *Appl Energ* 2015;148:121–33.

- [51] Korobenko A, Hsu M-C, Akkerman I, Bazilevs Y. Aerodynamic simulation of vertical-axis wind turbines. *J Appl Mech* 2013;81:021011. doi:10.1115/1.4024415.
- [52] Korobenko A, Hsu M-C, Akkerman I, Tippmann J, Bazilevs Y. Structural mechanics modeling and FSI simulation of wind turbines. *Math Model Method Appl Sci* 2013;23:249–72.
- [53] Lawson M, Li Y, Sale D. Development and verification of a computational fluid dynamics model of a horizontal-axis tidal current turbine. In: ASME 2011 30th international conference on ocean, offshore and arctic engineering. American Society of Mechanical Engineers; 2011. p. 711–20.
- [54] Lee J, Park S, Kim D, Rhee S, Kim M-C. Computational methods for performance analysis of horizontal axis tidal stream turbines. *Appl Energ* 2012;98:512–23.
- [55] Li Y, Calisal S. Three-dimensional effects and arm effects on modeling a vertical axis tidal current turbine. *Renew Energ* 2010;35(10):2325–34.
- [56] Liu P, Bose N. Prototyping a series of bi-directional horizontal axis tidal turbines for optimum energy conversion. *Appl Energ* 2012;99:50–66.
- [57] Malki R, Williams A, Croft T, Togneri M, Masters I. A coupled blade element momentum–computational fluid dynamics model for evaluating tidal stream turbine performance. *Appl Math Model* 2013;37(5):3006–20.
- [58] Masters I, Chapman J, Willis M, Orme J. A robust blade element momentum theory model for tidal stream turbines including tip and hub loss corrections. *J Marine Eng Technol* 2011;10(1):25–35.
- [59] Moghadam ME, Bazilevs Y, Hsia T-Y, Vignon-Clementel IE, Marsden AL, of Congenital Hearts Alliance (MOCHA) M. A comparison of outlet boundary treatments for prevention of backflow divergence with relevance to blood flow simulations. *Comput Mech* 2011;48:277–91. doi:10.1007/s00466-011-0599-0.
- [60] Osher S, Fedkiw R. *Level set methods and dynamic implicit surfaces*, 153. Springer Science and Business Media; 2006.
- [61] Osher S, Sethian JA. Fronts propagating with curvature-dependent speed: algorithms based on Hamilton–Jacobi formulations. *J Comput Phys* 1988;79(1):12–49.
- [62] Rispoli F, Corsini A, Tezduyar TE. Finite element computation of turbulent flows with the discontinuity-capturing directional dissipation (DCDD). *Comput Fluid* 2007;36:121–6. doi:10.1016/j.compfluid.2005.07.004.
- [63] Rourke FO, Boyle F, Reynolds A. Tidal energy update 2009. *Appl Energ* 2010;87(2):398–409.
- [64] Saad Y. A flexible inner-outer preconditioned GMRES algorithm. *SIAM J Sci Comput* 1993;14(2):461–9.
- [65] Saad Y, Schultz M. GMRES: A generalized minimal residual algorithm for solving nonsymmetric linear systems. *SIAM J Sci Stat Comp* 1986;7:856–69.
- [66] Takizawa K, Bazilevs Y, Tezduyar TE. Space–time and ALE-VMS techniques for patient-specific cardiovascular fluid–structure interaction modeling. *Arch Comput Meth Eng* 2012;19:171–225. doi:10.1007/s11831-012-9071-3.
- [67] Takizawa K, Bazilevs Y, Tezduyar TE, Hsu M-C, Øiseth O, Mathisen KM, et al. Engineering analysis and design with ALE-VMS and space–time methods. *Arch Comput Method Eng* 2014;21:481–508. doi:10.1007/s11831-014-9113-0.
- [68] Takizawa K, Bazilevs Y, Tezduyar TE, Long CC, Marsden AL, Schjodt K. ST and ALE-VMS methods for patient-specific cardiovascular fluid mechanics modeling. *Math Model Method Appl Sci* 2014;24:2437–86. doi:10.1142/S0218202514500250.
- [69] Takizawa K, Henicke B, Montes D, Tezduyar TE, Hsu M-C, Bazilevs Y. Numerical-performance studies for the stabilized space–time computation of wind-turbine rotor aerodynamics. *Comput Mech* 2011;48:647–57. doi:10.1007/s00466-011-0614-5.
- [70] Takizawa K, Henicke B, Puntel A, Kostov N, Tezduyar TE. Computer modeling techniques for flapping-wing aerodynamics of a locust. *Comput Fluid* 2013;85:125–34. doi:10.1016/j.compfluid.2012.11.008.
- [71] Takizawa K, Henicke B, Tezduyar TE, Hsu M-C, Bazilevs Y. Stabilized space–time computation of wind-turbine rotor aerodynamics. *Comput Mech* 2011;48:333–44. doi:10.1007/s00466-011-0589-2.
- [72] Takizawa K, Montes D, McIntyre S, Tezduyar TE. Space–time VMS methods for modeling of incompressible flows at high Reynolds numbers. *Math Model Method Appl Sci* 2013;23:223–48. doi:10.1142/S0218202513400022.
- [73] Takizawa K, Tanizawa K, Yabe T, Tezduyar TE. *Computational ship hydrodynamics with the CIP method*. Marine 2007. Onate E, Garcia J, Bergan P, Kvamsdal T, editors. Barcelona, Spain: CIMNE; 2007.
- [74] Takizawa K, Tanizawa K, Yabe T, Tezduyar TE. Ship hydrodynamics computations with the CIP method based on adaptive Soroban grids. *Int J Numer Method Fl* 2007;54:1011–19. doi:10.1002/flid.1466.
- [75] Takizawa K, Tezduyar TE. Multiscale space–time fluid–structure interaction techniques. *Comput Mech* 2011;48:247–67. doi:10.1007/s00466-011-0571-z.
- [76] Takizawa K, Tezduyar TE. Space–time fluid–structure interaction methods. *Math Model Method Appl Sci* 2012;22(supp02):1230001. doi:10.1142/S0218202512300013.
- [77] Takizawa K, Tezduyar TE, Buscher A. Space–time computational analysis of MAV flapping-wing aerodynamics with wing clapping. *Comput Mech* 2015;55:1131–41. doi:10.1007/s00466-014-1095-0.
- [78] Takizawa K, Tezduyar TE, Buscher A, Asada S. Space–time fluid mechanics computation of heart valve models. *Comput Mech* 2014;54:973–86. doi:10.1007/s00466-014-1046-9.
- [79] Takizawa K, Tezduyar TE, Hattori H. Computational analysis of flow-driven string dynamics in turbomachinery. *Comput Fluid March* 2016. published online doi: 10.1016/j.compfluid.2016.02.019.
- [80] Takizawa K, Tezduyar TE, Kostov N. Sequentially-coupled space–time FSI analysis of bio-inspired flapping-wing aerodynamics of an MAV. *Comput Mech* 2015;55:2227–55. doi:10.1007/s00466-014-0980-x.
- [81] Takizawa K, Tezduyar TE, Kuraishi T. Multiscale ST methods for thermo–fluid analysis of a ground vehicle and its tires. *Math Model Method Appl Sci* 2015;25:2227–55. doi:10.1142/S0218202515400072.
- [82] Takizawa K, Tezduyar TE, Kuraishi T, Tabata S, Takagi H. Computational thermo–fluid analysis of a disk brake. *Computational Mechanics February* 2016. published online doi: 10.1007/s00466-016-1272-4.
- [83] Takizawa K, Tezduyar TE, McIntyre S, Kostov N, Kolesar R, Habluetzel C. Space–time VMS computation of wind-turbine rotor and tower aerodynamics. *Comput Mech* 2014;53:1–15. doi:10.1007/s00466-013-0888-x.
- [84] Takizawa K, Tezduyar TE, Mochizuki H, Hattori H, Mei S, Pan L, et al. Space–time VMS method for flow computations with slip interfaces (ST-SI). *Math Model Method Appl Sci* 2015;25:2377–406. doi:10.1142/S0218202515400126.
- [85] Takizawa K, Tezduyar TE, Otoguro Y, Terahara T, Kuraishi T, Hattori H. Turbocharger flow computations with the space–time isogeometric analysis (ST-IGA). *Comput Fluids March* 2016. published online doi: 10.1016/j.compfluid.2016.02.021.
- [86] Tezduyar TE. Finite element methods for flow problems with moving boundaries and interfaces. *Arch Comput Method E* 2001;8:83–130. doi:10.1007/BF02897870.
- [87] Tezduyar TE. Computation of moving boundaries and interfaces and stabilization parameters. *Int J Numer Method Fl* 2003;43:555–75. doi:10.1002/flid.505.
- [88] Tezduyar TE. Finite elements in fluids: stabilized formulations and moving boundaries and interfaces. *Comput Fl* 2007;36:191–206. doi:10.1016/j.compfluid.2005.02.011.
- [89] Tezduyar TE, Sathe S. Modeling of fluid–structure interactions with the space–time finite elements: Solution techniques. *Int J Numer Method Fl* 2007;54:855–900. doi:10.1002/flid.1430.
- [90] Wang C, Wu MC-H, Xu F, Hsu M-C, Bazilevs Y. Modeling of a hydraulic arresting gear using fluid–structure interaction and isogeometric analysis. *Comput Fl* 2015. Published online doi: 10.1016/j.compfluid.2015.12.004.
- [91] Yan J, Augier B, Korobenko A, Czarnowski J, Ketterman G, Bazilevs Y. FSI modeling of a propulsion system based on compliant hydrofoils in a tandem configuration. *Comput Fl* 2015. Published online doi: 10.1016/j.compfluid.2015.07.013.
- [92] Yan J, Korobenko A, Deng X, Bazilevs Y. Computational free-surface fluid–structure interaction with application to floating offshore wind turbines. *Comput Fluids* 2016. Published online doi: 10.1016/j.compfluid.2016.03.008.